Results in Engineering 32 (2026) 113014

Contents lists available at ScienceDirect

Results in Engineering

journal homepage: www.sciencedirect.com/journal/results-in-engineering

Research paper

# Auxetic mechanical metamaterials for strain amplification

Sakineh Fotouhi [a], Fahad Mohammed [b], Fadi Jaber [c,d], Mohammad Fotouhi [e,*]

[a] School of Engineering, University of the West of England, Bristol, United Kingdom
[b] Bristol Composites Institute, University of Bristol, United Kingdom
[c] Department of Biomedical Engineering, Ajman University, Ajman, United Arab Emirates
[d] Center of Medical and Bio-allied Health Sciences Research, Ajman University, Ajman, United Arab Emirates
[e] Faculty of Civil Engineering and Geosciences, Delft University of Technology, Delft, 2628CD, the Netherlands

ARTICLE INFO

*Keywords:*
Mechanical metamaterials
Auxetic lattices
Strain amplification
Finite element analysis

ABSTRACT

Mechanical metamaterials can amplify deformation through geometry-driven mechanisms, transforming small global strains into localized regions of enhanced strain without altering the constituent material. This capability is attractive for applications requiring controlled deformation and mechanical responsiveness, including sensing, actuation, energy harvesting, and adaptive structures. Although numerous auxetic lattice architectures have been proposed, their reported mechanical performances are difficult to compare because previous studies have employed different material models, geometric definitions, loading conditions, and evaluation methodologies. Consequently, quantitative design guidelines for selecting the most appropriate architecture remain limited. This study addresses this gap through a unified finite element framework that systematically compares four representative auxetic lattice architectures (re-entrant, star-shaped, arrowheaded, and chiral) under identical material properties, geometric scaling, boundary conditions, loading conditions, and performance metrics. A hyperelastic poly(butylene adipate-co-terephthalate) constitutive model was used to investigate 36 geometric configurations by varying cell angle and structural thickness. Mechanical performance was evaluated in terms of strain amplification factor (SAF), effective Poisson's ratio, effective stiffness, stress distribution, and relative density. The results reveal pronounced architecture-dependent trade-offs, with lattice topology producing nearly a six-fold variation in strain amplification (SAF $\approx$ 1.4–8). The star-shaped and re-entrant lattices achieved the highest strain amplification, whereas the arrowheaded lattice consistently exhibited the lowest strain amplification but the highest stiffness and most negative effective Poisson's ratio. The resulting Ashby-style performance maps are reported to establish a quantitative design framework for balancing strain amplification, auxeticity, stiffness, and lightweighting, providing practical guidance for selecting auxetic lattice architectures according to application-specific mechanical requirements.

## 1. Introduction

Mechanical metamaterials are a class of architected materials whose effective mechanical response is governed primarily by structural geometry rather than the intrinsic properties of their constituent materials. By carefully designing the architecture of repeating unit cells, these materials can exhibit extraordinary behaviours that are difficult or impossible to achieve in conventional solids, including negative Poisson's ratio, programmable stiffness, shape morphing, negative compressibility, enhanced energy absorption, and tunable deformation pathways [1–3]. Advances in additive manufacturing and computational design have accelerated the development of mechanical metamaterials over the past two decades, enabling the realization of increasingly complex architectures across multiple length scales and application domains [2–5].

Auxetic metamaterials have attracted significant attention due to their counterintuitive deformation behaviour, exhibiting a negative Poisson's ratio [6–11]. Previous studies have shown that auxetic structures can exhibit enhanced indentation and impact resistance, increased fracture toughness, superior shear resistance, improved energy absorption capacity, synclastic curvature under bending, and enhanced damage tolerance compared with conventional cellular materials. These characteristics have motivated their application in aerospace structures, protective systems, biomedical implants, flexible electronics, robotics,

* Corresponding author.
*E-mail address:* m.fotouhi-1@tudelft.nl (M. Fotouhi).

https://doi.org/10.1016/j.rineng.2026.113014
Received 4 July 2026; Received in revised form 9 August 2026; Accepted 14 September 2026
Available online 15 September 2026

wearable devices, and adaptive structural systems [10,12–14]. Recent studies further demonstrate the transition of auxetic metamaterials from conceptual designs toward application-oriented systems [15]. For example, auxetic structures have recently been incorporated into wearable strain sensors to provide conformal, multidirectional deformation and stable sensing during human motion [16]. Similarly, Liu et al [17] developed an auxetic triboelectric nanogenerator that exploits the negative Poisson's ratio and synclastic deformation of the structure to improve mechanical compatibility with human joints and enable motion monitoring in wearable devices. In the biomedical field, recent advances in additive manufacturing have enabled the fabrication of complex auxetic architectures for biomedical devices, where their tunable mechanical response and geometric conformability offer advantages for patient-specific applications [18].

Strain amplification is a key functional characteristic of auxetic mechanical metamaterials. It refers to the ability of a metamaterial to convert relatively small global deformations into substantially larger local strains within targeted regions through geometric design. Unlike conventional strategies that enhance performance by modifying material composition or incorporating highly sensitive sensing elements, strain amplification exploits structural geometry to intensify the local mechanical response [19–24]. Strain amplification is particularly relevant to applications involving sensing, actuation, energy harvesting, and adaptive systems. For example, strain sensors often rely on local deformation to generate measurable electrical, optical, or mechanical signals. By concentrating deformation into specific regions, metamaterial architectures can enhance sensor sensitivity while maintaining relatively small overall structural deformation. Similar advantages have been demonstrated in piezoresistive sensors, triboelectric energy harvesters, fibre-optic sensors, and mechanochromic materials, where geometry-induced strain amplification enhances signal generation, sensing sensitivity, and energy conversion efficiency [25–28].

Recent studies have highlighted the potential of auxetic architectures as effective strain amplification mechanisms. For example, Lee et al. developed auxetic photonic patterns capable of generating ultrasensitive mechanochromic responses through architecture-induced strain amplification, achieving 20 times higher sensitivity than bulk photonic films [19]. Their study demonstrated that carefully designed auxetic cut patterns could amplify local strains by an order of magnitude, enabling enhanced colour change under relatively small global deformation. Similar concepts have been explored in stretchable photonic materials, strain amplification for composite material monitoring, flexible electronics, and adaptive sensing systems, where localized strain concentration substantially improves functional performance [22–28].

Although numerous auxetic structures have been proposed for strain amplification, selecting an appropriate architecture for a given application remains challenging because their mechanical performance is strongly dependent on structural geometry. Different structures exhibit distinct combinations of Poisson's ratio, stiffness, deformation capability, stress distribution, and strain amplification, resulting in application-specific performance trade-offs. Understanding how structure influences these competing characteristics is therefore essential for the rational design of auxetic metamaterials. Among the many auxetic architectures reported in the literature, re-entrant, chiral, arrowheaded, and star-shaped lattices are among the most widely studied and representative structure families [9,10,14]. These architectures employ different deformation mechanisms, including rib hinging, ligament bending, and rotational kinematics, to achieve negative Poisson's ratio behaviour and exhibit distinctly different mechanical characteristics.

Despite extensive research on auxetic metamaterials for strain amplification, systematic comparisons of representative auxetic architectures under consistent evaluation conditions remain limited. Most existing studies investigate a single lattice topology and employ different finite element modelling assumptions, including material constitutive models, geometric definitions, boundary conditions, loading protocols, and performance evaluation methods, making direct comparison between reported results difficult. Consequently, it remains unclear whether observed differences in mechanical performance arise from the structural architecture itself or from inconsistencies in the evaluation methodology. Furthermore, although the effective Poisson's ratio is the most frequently reported performance metric, it alone is insufficient for evaluating strain-amplifying metamaterials. Mechanical performance is inherently multi-objective, with strain amplification, stiffness, stress distribution, and auxeticity exhibiting competing trade-offs. A systematic parametric comparison of representative auxetic architectures under a unified modelling framework is therefore essential for establishing quantitative design guidelines for application-specific design.

To address this need, this study presents a comparative finite element investigation of four representative auxetic lattice architectures: re-entrant, star-shaped, arrowheaded, and chiral. Fig. 1 illustrates the four lattice structures together with their normalized cross-sectional areas relative to a fully solid material for the selected geometric configurations. All architectures are evaluated using identical material properties, geometric scaling, boundary conditions, loading conditions, and performance metrics, enabling a direct and unbiased comparison of their mechanical response. The study establishes a quantitative basis for assessing the trade-offs between strain amplification, effective Poisson's ratio, stiffness, and stress distribution, while the resulting multi-objective performance maps provide practical design guidelines for selecting auxetic architectures according to application-specific requirements.

## 2. Methodology

### 2.1. Model development and validation

A 3D finite element model was developed using Abaqus/CAE 2025 (Dassault Systèmes SIMULIA) on the licensed installation at the University of Bristol, Bristol, UK. The mechanical behaviour of representative auxetic lattice structures is investigated under uniaxial tensile loading. The modelling procedure comprised three stages: (i) validation of the finite element model against published numerical results, (ii) a systematic parametric investigation of four representative auxetic lattice architectures, and (iii) evaluation of strain amplification factor (SAF), effective Poisson's ratio, effective stiffness, and stress distribution.

Prior to the parametric investigation, the finite element model was validated against the results reported by Schneider et al [29] for a re-entrant auxetic structure with a cell angle of 50°. The same 5 × 5 cell arrangement, polybutylene adipate terephthalate (PBAT) Ogden N = 4 material model, boundary conditions, and out-of-plane extrusion depth of 2.5 mm were adopted, consistent with the reference study. The

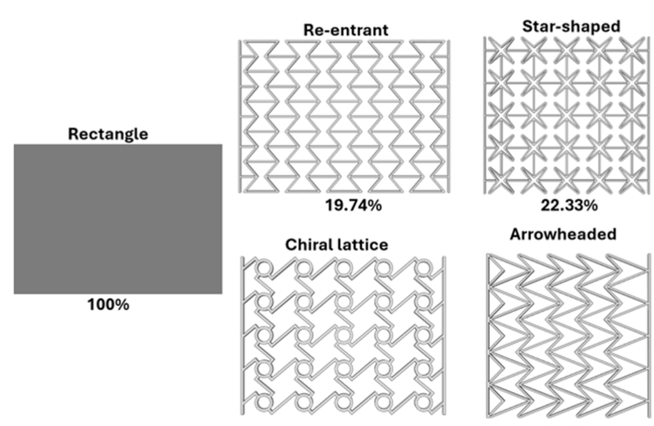


**Fig. 1.** Representative auxetic lattice structures and normalized cross-sectional areas considered in this study.

effective Poisson's ratio was also calculated using the same approach used by Schneider et al [29], whereby five node pairs from each of the three middle rows (rows 2, 3, and 4) of the 5 × 5 arrangement, as shown in Fig. 8, were tracked to determine the transverse strain, which was subsequently combined with the applied longitudinal strain to compute the effective Poisson's ratio. This approach minimises the influence of boundary-induced deformation effects on the calculated Poisson's ratio, as the outer rows are disproportionately affected by the applied boundary conditions, consistent with the observation of Schneider et al [29].

A mesh sensitivity study was conducted to ensure mesh-independent results. Peak von Mises stress was selected as the convergence criterion because of its sensitivity to the local stress concentrations that develop junctions. Schneider et al [29] employed a nominal element edge size of approximately 0.2 mm with local variations around the strut junctions. As detailed unit-cell geometry and meshing strategies are not fully reported in the literature, the mesh employed in the present work was selected based on the demonstrated convergence of the numerical solution rather than attempting to replicate the reference mesh directly. C3D8H hybrid hexahedral elements were evaluated using global mesh sizes of 0.5, 0.4, and 0.3 mm. The predicted stresses were compared with the reference value of 1.463 MPa at 3.37% global strain reported by Schneider et al [29]. The predicted von Mises stress decreased from 1.490 MPa for the 0.5 mm mesh to 1.434 MPa for the 0.4 mm mesh, with only a marginal change to 1.435 MPa for the 0.3 mm mesh. The relative difference between the two finest meshes was <0.1%, indicating that further mesh refinement produced a negligible change in the predicted stress. The predicted stress values differed by <2% from the published reference value, providing additional confidence in the accuracy of the adopted modelling approach. The mesh convergence results are presented in Fig. 2, and the agreement between the predicted stress distribution and deformation pattern is demonstrated in Fig. 3. As shown in Fig. 3, the present model reproduces the increasing trends in both the force–displacement response and strain-dependent Poisson's ratio of the re-entrant auxetic structure reported by Schneider et al [29]. For comparison with the published 10 mm-thick specimen, the FE-predicted reaction forces were scaled by a factor of four, resulting in close agreement with the reference force magnitude. The predicted Poisson's ratio also agrees well with the reference data, with a mean relative deviation of approximately 4.2% (2.9–5.3%) over the strain range of 0.5–5.0%. This small deviation is consistent with the thickness-dependent variations observed in the present parametric study (Fig. 9). Consequently, a global mesh size of 0.3 mm with C3D8H elements was adopted from verification of the re-entrant structure. In addition to peak stress and deformation pattern, the poisson's ratio evolution was compared with the corresponding finite element results reported by Schneider et al [29], as presented in Fig. 3b.

The same mesh size and elements type were examined for all the other structures. However, for the chiral lattice and arrowheaded structures, C3D8H hexahedral elements produce poorly conditioned mesh at the circular nodes and sharp convergent tips respectively, as shown in Fig. 4, and were therefore replaced with C3D10H quadratic tetrahedral elements. A global mesh size of 0.3 was adopted consistently

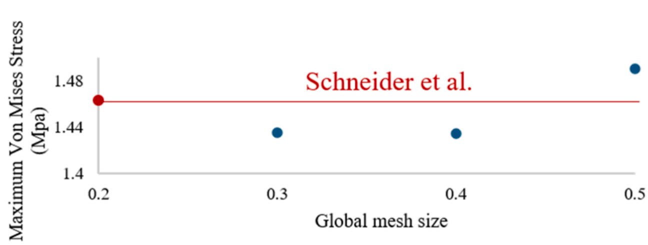


**Fig. 2.** Mesh convergency study for the 50° re-entrant auxetic structure, and the associated maximum Von Mises stress compared with the work by Schneider et al [29].

across all four structures as the finest mesh balancing numerical resolution with computational limitations.

### 2.2. Simulation setup

Following model validation, four auxetic lattice structures, namely re-entrant, chiral, arrowheaded, and star-shaped lattices, were investigated. For each structure, a unit cell was developed and repeated in a 5 × 5 arrangement to maintain consistency with the validated literature. The investigated structures and the geometric parameters defining each unit cell are shown in Fig. 5. For all four structures, the cell angle (θ) was varied systematically from 50° to 55° and 60°. Two out-of-plane thicknesses (t = 1.5 mm, 2.0 mm, and 2.5 mm) were also considered, resulting in a total of 36 finite element simulations (4 structures × 3 cell angles × 2 thicknesses). As the overall dimensions of each structure vary with unit cells geometry and cell angle, the relative density (defined as the ratio of the solid area to the overall area, expressed as a percentage) was calculated to enable meaningful comparisons of mechanical performance. Fig. 5 illustrates the representative unit-cell geometries at a cell angle of 50°, providing a visual reference for the geometric configuration and angle definition. Since the influence of thickness is normalised in the relative density calculation, only the 12 unique structure-angle combinations are summarised in Table 1. The in-plane wall width was maintained constant at 0.8 mm throughout the study, consistent with the validation study. To ensure a direct comparison between structures and geometric configurations, the material properties, element formulation and mesh size (see Fig. 6), boundary conditions, and post-processing methods were maintained throughout the simulations, with these parameters chosen based on the validation section.

The structures were modelled using PBAT. Here, the material behaviour was represented using the four-term Ogden hyperelastic method. The material parameters were adopted directly from literature Schneider et al [29], where the model was calibrated against experimental uniaxial tensile test data on PBAT (Ecoflex F Blend C1200) in accordance with DIN EN ISO 527–1. The calibrated material constants used in the present study are summarised in Table 2.

The boundary conditions applied to all structures is as shown in Fig. 7 and is the same for all structures. One edge of each lattice structure was fully constrained, while a displacement controlled tensile load was applied to the opposite edge along the longitudinal direction.

Previous studies have shown that the deformation behaviour of auxetic structures is governed by geometric changes within the unit cell, making geometrically non-linear formulations necessary for accurate representation of their mechanical response [30,31]. Therefore, all the simulations were performed using the Standard Static General solver of Abaqus/CAE 2025 (Dassault Systèmes SIMULIA) with geometric non-linearity enabled (NLGEOM = ON) to capture the large deformations, ligament bending, cell rotation, and geometric reconfiguration associated with auxetic deformation.

### 2.3. Performance evaluation

The effects of cell angle and out-of-plane thickness on SAF, effective Poisson's ratio, effective stiffness, and stress distribution were studied. Stress distributions were evaluated using von Mises stress contours to identify stress concentration regions and assess the influence of geometric parameters on the deformation behaviour of all four structures. In accordance with previous works [29,32], the effective Poisson's ratio was calculated using $\nu = -\frac{\varepsilon_y}{\varepsilon_x}$, where $\varepsilon_x$ and $\varepsilon_y$ are the longitudinal and transverse engineering strains. The measurements were obtained from the three middle rows of the 5 × 5 lattice arrangement (row 2,3, and 4) to minimise boundary induced deformation effects [29]. Five nodes location were tracked in each row, resulting in a total of 15 measurement points as shown in Fig. 8. The average transverse displacement

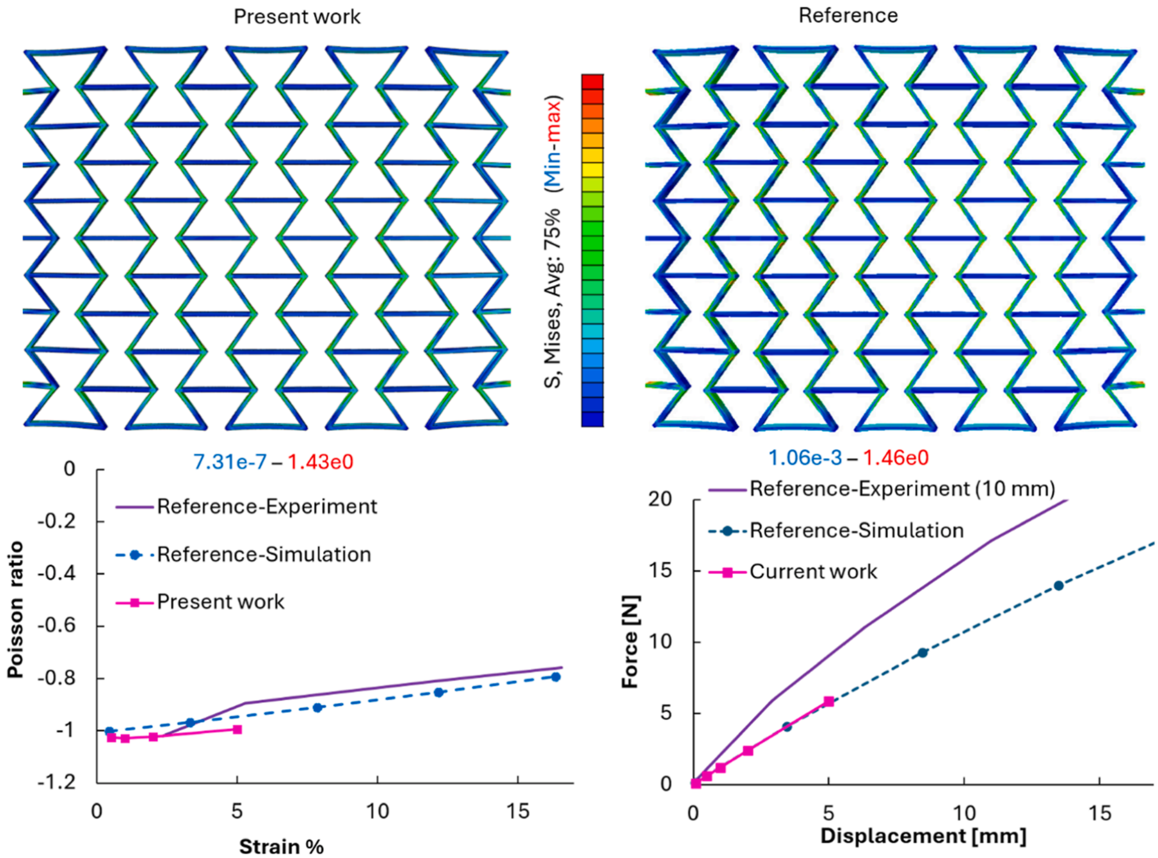


**Fig. 3.** Verification of the FEM, Predicted von Mises stress, deformation pattern, Poisson's ratio, and force displacement comparison.

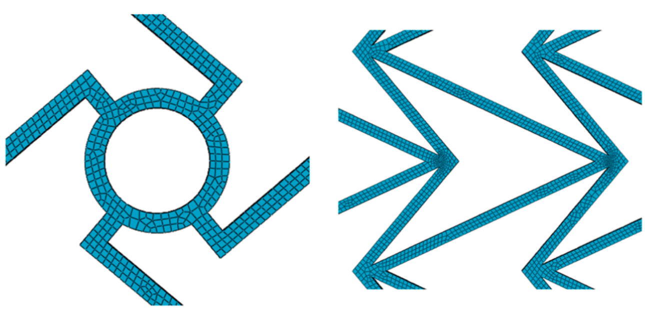

**Fig. 4.** Initial mesh distribution at 0.3 mm mesh size of C3D8H for (a) Chiral lattice and (b) Arrowheaded.

obtained from these locations was used to calculate the effective transverse strain, which was subsequently combined with the longitudinal strain to determine the effective Poisson's ratio.

SAF was used to quantify the ability of each auxetic structure to amplify local deformation relative to the applied global strain was calculated using Eq. (1).

$$SAF = \frac{\varepsilon_{local}}{\varepsilon_{global}} \tag{1}$$

Where $\varepsilon_{local}$ is the local strain measured between two selected locations (as shown earlier in Fig. 5) and $\varepsilon_{global}$ is the applied global strain. The local strain was calculated as the change in the distance between the selected nodes divided by their initial separation.

$$\varepsilon_{\text{local}} = \frac{\Delta(\text{distance between selected nodes})}{\text{initial distance between selected nodes}} \tag{2}$$

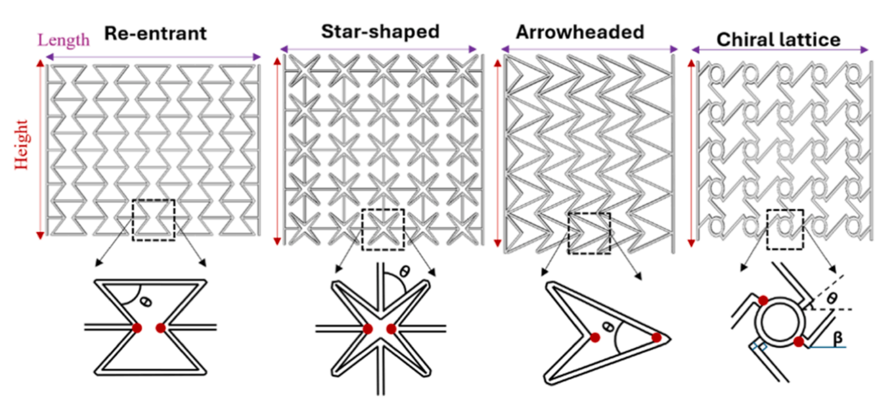


**Fig. 5.** Auxetic structures and parameters (marked locations are used for calculating SAF).

**Table 1**
Geometric parameters considered in the parametric investigation.

| Type of structure | Re-entrant | | | Star-shaped | | | Chiral lattice | | | Arrowheaded | | |
|---|---|---|---|---|---|---|---|---|---|---|---|---|
| $\theta^0$ | 50° | 55° | 60° | 50° | 55° | 60° | 50° | 55° | 60° | 50° | 55° | 60° |
| Length (mm)<br>x<br>Height (mm) | 105.81<br>x<br>76.80 | 105.76<br>x<br>76.80 | 105.8<br>x<br>76.80 | 102.22<br>x<br>96.42 | 101.17<br>x<br>96.46 | 100.97<br>x<br>96.30 | 69.14<br>x<br>53.42 | 76.83<br>x<br>50.69 | 86.89<br>x<br>48.54 | 68.68<br>x<br>80.37 | 69.22<br>x<br>95.94 | 69.35<br>x<br>115.52 |
| Relative Density (%) | 19.75 | 18.66 | 17.69 | 22.34 | 20.61 | 19.39 | 22.6 | 21.79 | 20.75 | 23.26 | 21.99 | 21 |

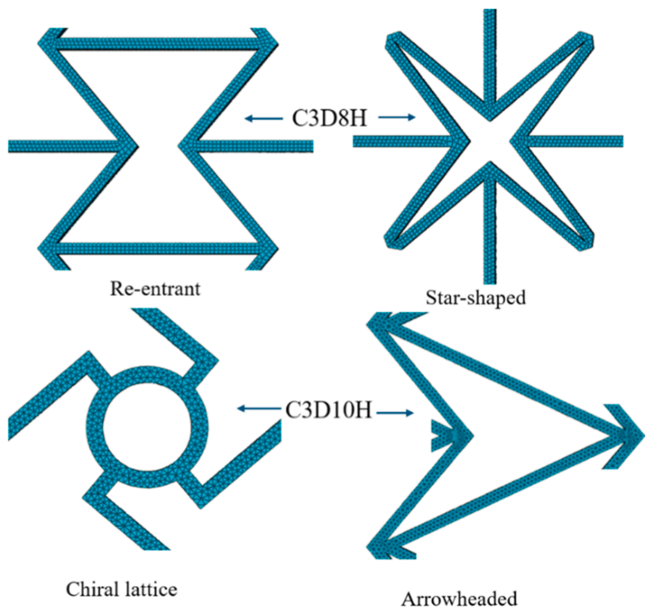


**Fig. 6.** Mesh representation of the unit cell for all structures at an angle of 50° with 0.3 mm mesh size.

**Table 2**
Ogden hyperelastic material parameters for PBAT adopted from Schneider et al [29].

| Parameter | Value | Parameter | Value | Parameter | Value |
|---|---|---|---|---|---|
| N | 4 | $\nu$ | 0.41 | - | - |
| $\alpha_1$ | 5.2798 | $\mu_1$ | −32.7303 | $D_1$ | 0.01,112 |
| $\alpha_2$ | 5.2803 | $\mu_2$ | 1.7398 | $D_2$ | 0 |
| $\alpha_3$ | −1.0637 | $\mu_3$ | 3.5032 | $D_3$ | 0 |
| $\alpha_4$ | −10.5607 | $\mu_4$ | 61.9267 | $D_4$ | 0 |

* μ1, μ2, μ3, and μ4 are in [MPa] and D1, D2, D3, and D4 are in [MPa-1].

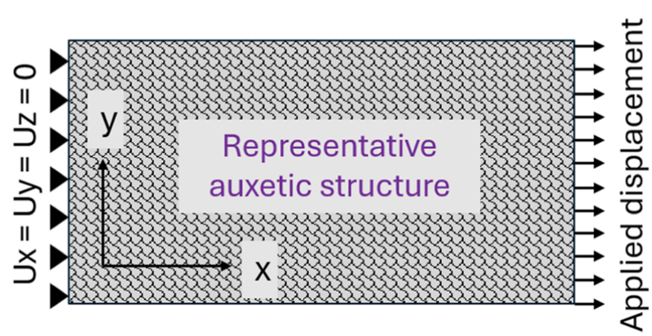


**Fig. 7.** Boundary conditions used in the finite element analysis.

The selected nodes were located within the central cell, a high strain concentration region identified from preliminary deformation analyses, thereby providing a representative measure of local strain amplification.

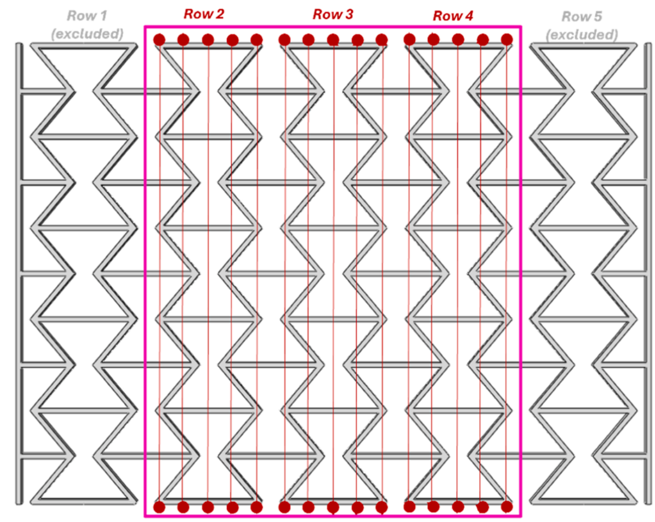


**Fig. 8.** Measurement locations used for effective Poisson's ratio calculation [29].

The effective stiffness of each lattice structure was determined using Eq. (3).

$$K = \frac{F}{\Delta} \tag{3}$$

Where F is the total force obtained from the simulation resulted from Δ, i.e. the prescribed displacement applied during tensile loading. The reaction force was extracted from a reference point assigned the entire central cell.

## 3. Results and discussion

A preliminary strain sensitivity analysis was conducted on re-entrant and star-shaped auxetic lattices to establish an appropriate global strain for the parametric study. Global strain levels of 0.1%, 0.5%, 1%, 2%, and 5% were applied to re-entrant and star-shaped structure, and the corresponding SAF was evaluated over the investigated strain range. As shown in Fig. 9, the SAF increased slightly between 0.1% and 0.5% global strain. Beyond 0.5% global strain, only minor variations in the SAF were observed despite ten times increase in applied global strain. Between 0.5% and 1% global strain, the SAF increased by only 0.55% for the re-entrant lattice and 0.16% for the star-shaped lattice. Similarly, increasing the global strain from 1% to 2% resulted in SAF increases of only 1.07% and 0.06% for the re-entrant and star-shaped lattices, respectively. These results indicate that further increase in applied global strain have little influence on the stain amplification response. Consequently, a global strain of 1% was selected as the representative loading conditions for all subsequent simulations.

The effects of cell angle and out-of-plane thickness on the SAF, effective Poisson's ratio, and effective stiffness of the four auxetic lattice structures are presented below. Based on the strain sensitivity analysis described in Section 2.3, all results correspond to an applied global strain of 1%. Representative deformation configurations and corresponding von Mises stress distributions for each architecture at a cell

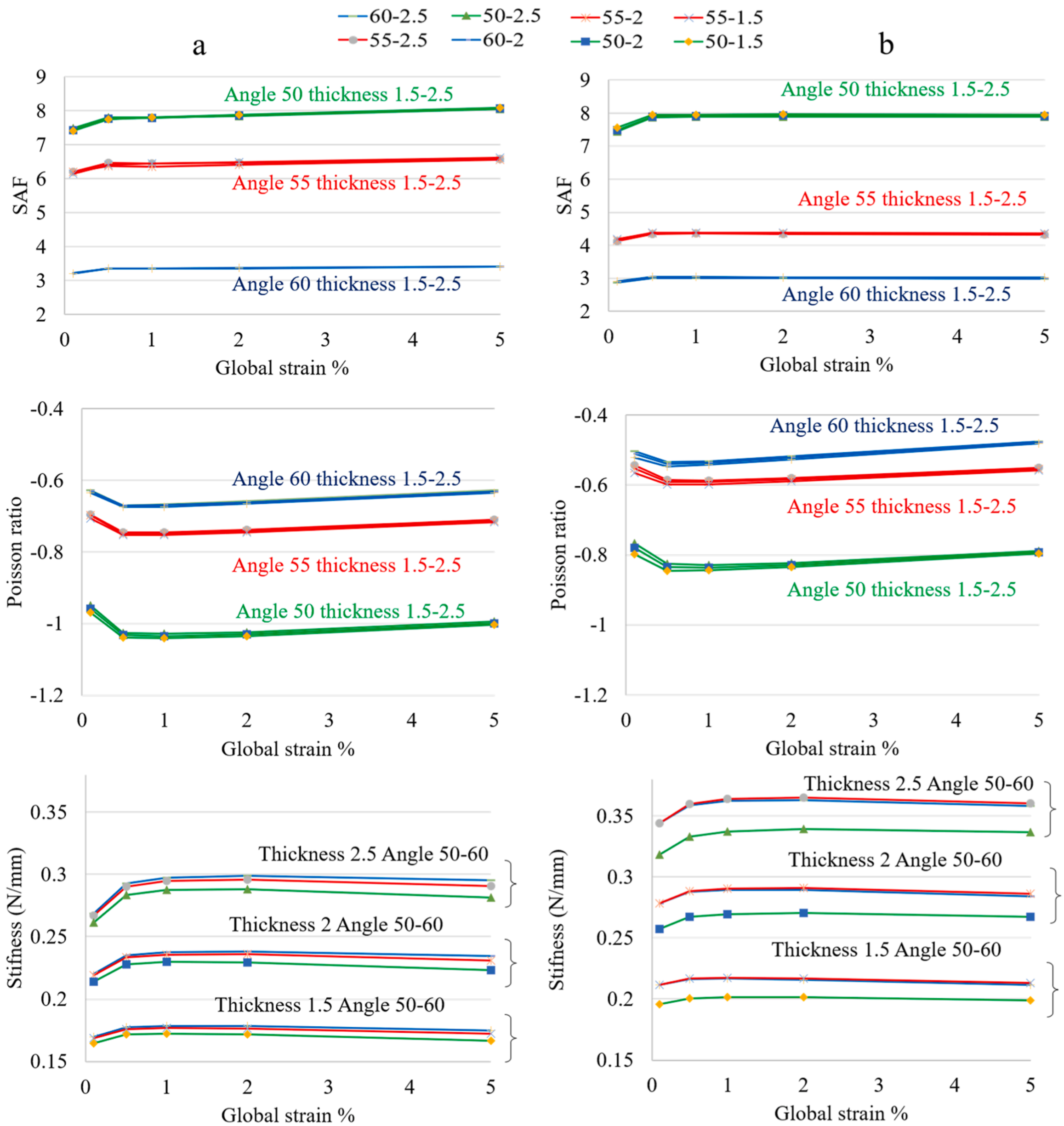


**Fig. 9.** Variation of the SAF, Poisson ration, and stiffness with increasing global strain for (a) re-entrant and (b) star-shaped structures.

angle of 50° are shown in Fig. 10 using a deformation magnification factor of 5.

As the primary performance metric considered in this study, the calculated SAF values for all four auxetic architectures are summarised in Table 3. The results demonstrate that cell angle has a substantially greater influence on strain amplification than out-of-plane thickness. Across the investigated thickness range (1.5–2.0 mm), only negligible changes were observed for all structures, indicating that strain amplification is governed predominantly by the in-plane unit-cell geometry rather than the out-of-plane dimension.

The results in Table 3 demonstrate that the four auxetic architectures exhibit markedly different strain amplification responses to changes in cell angle. The re-entrant and star-shaped lattices consistently achieved the highest SAF values, whereas the chiral and arrowheaded lattices exhibited substantially lower amplification. Furthermore, opposite trends with increasing cell angle were observed: the SAF decreased for the re-entrant and star-shaped lattices but increased for the chiral and arrowheaded architectures, indicating that strain amplification is strongly dependent on the underlying deformation mechanism.

The re-entrant and star-shaped lattices exhibited the highest strain amplification, with both showing a pronounced reduction as the cell angle increased. For the re-entrant lattice, the maximum SAF of 7.80 was obtained at 50°, decreasing to 3.35 at 60°, corresponding to a reduction of approximately 57%. Similarly, the star-shaped lattice achieved a maximum SAF of 7.95 at 50°, decreasing to 3.03 at 60°, representing a reduction of approximately 62%. This behaviour reflects the similar deformation mechanisms of the two architectures. Smaller cell angles promote greater ligament bending and rotation during tensile loading, allowing larger geometric reconfiguration of the unit cell, consistent with the established deformation mechanism of re-entrant auxetic lattices [33,34]. Consequently, the larger relative displacement between the selected measurement nodes produces higher local strain and therefore greater strain amplification.

In contrast, the chiral lattice exhibited an increasing trend in SAF with increasing cell angle, rising from 1.91 at 50° to 2.59 at 60°, corresponding to an increase of approximately 36%. Unlike the re-entrant and star-shaped lattices, deformation in the chiral architecture is governed primarily by ligament rotation. Increasing the cell angle enhances

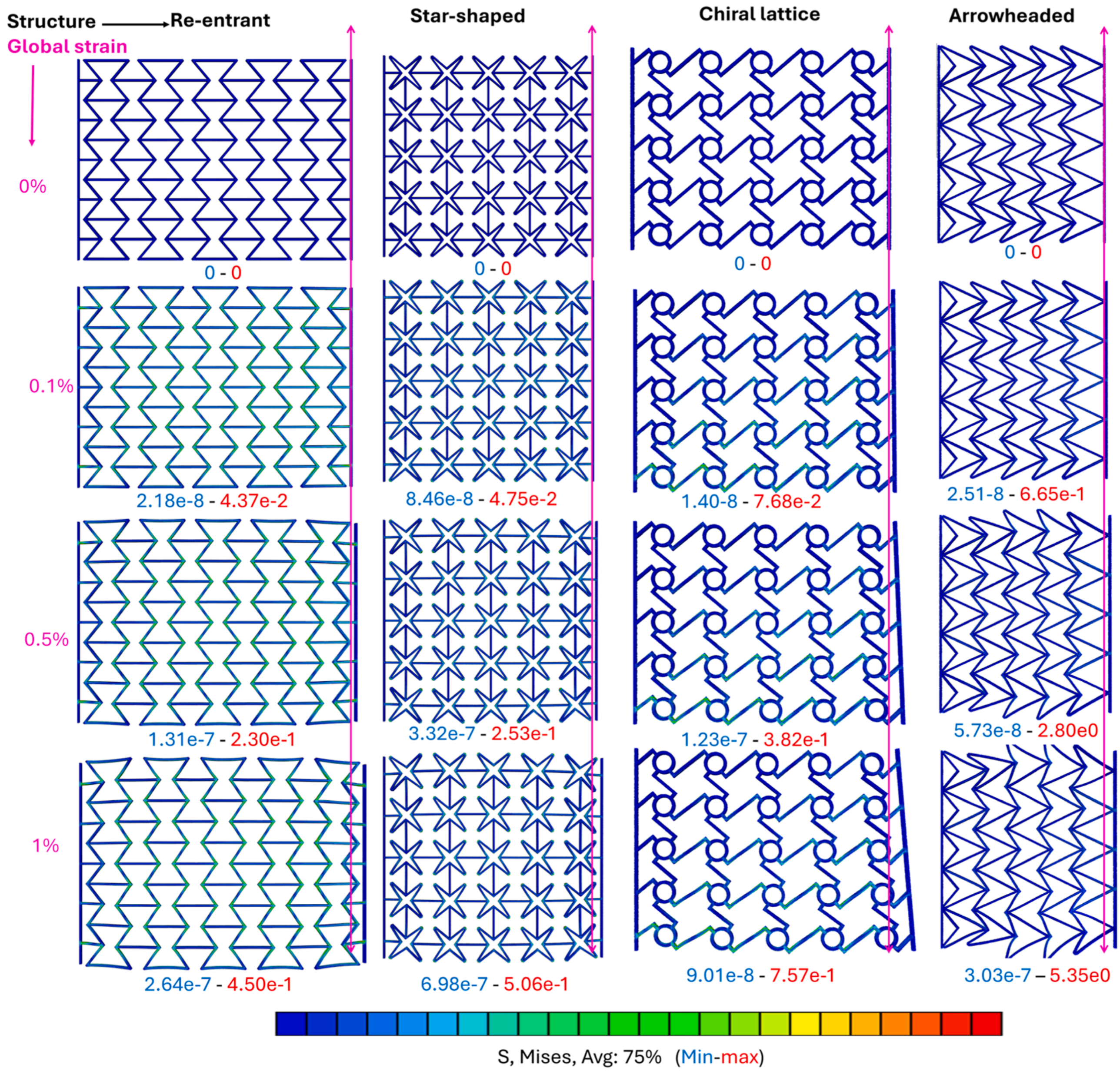


**Fig. 10.** A representative deformation progress and stress distribution for each structure at 50°.

**Table 3**
SAF values for all four structures across all cell angles and thickness.

| Structure | Thickness / Cell angle | 1.5 mm | 2.0 mm | 2.5 mm |
|---|---|---|---|---|
| Re-entrant | 50° | 7.80 | 7.79 | 7.80 |
| | 55° | 6.44 | 6.35 | 6.44 |
| | 60° | 3.35 | 3.34 | 3.35 |
| Star-shaped | 50° | 7.95 | 7.91 | 7.88 |
| | 55° | 4.48 | 4.36 | 4.35 |
| | 60° | 3.03 | 3.02 | 3.01 |
| Chiral lattice | 50° | 1.91 | 1.90 | 1.89 |
| | 55° | 2.18 | 2.17 | 2.16 |
| | 60° | 2.59 | 2.58 | 2.57 |
| Arrowheaded | 50° | 1.40 | 1.38 | 1.38 |
| | 55° | 1.41 | 1.40 | 1.39 |
| | 60° | 2.05 | 2.02 | 2.01 |

this rotational mechanism, producing larger relative displacements between the selected measurement nodes and consequently higher local strain. The asymmetric deformation observed in Fig. 10 is characteristic of chiral lattices and results from the coupling between the applied tensile strain and internal ligament rotation [35–37]. This interpretation is further supported by the von Mises stress contours, which show stress concentrations at the ligament-node junctions, indicating that deformation is accommodated predominantly through bending and rotational kinematics rather than uniform axial stretching.

The arrowheaded lattice exhibited the lowest strain amplification among the four architectures. The SAF remained almost unchanged between 50° and 55°, varying by <1%, before increasing to 2.05 at 60°. The deformation behaviour of cellular structures is governed by the relative contributions of flexure, stretching, and hinging, which are dependent on the unit cell geometry [33,34,37]. As observed from the deformation configuration, the arrowheaded unit cells undergo ligament bending and rotation under tensile loading while largely retaining their overall geometry at 1% global strain. Consequently, the change in distance between the selected measurement nodes remains relatively small, which results in low SAF. The increase in SAF at cell angle of 60° suggests that the larger cell angle permits greater ligament deformation, leads to an increase in SAF.

Overall, the results demonstrate that strain amplification is governed primarily by the dominant deformation mechanism and unit-cell geometry of the lattice, with cell angle being the most influential geometric parameter and out-of-plane thickness having only a negligible effect over the investigated range. Architectures that undergo substantial geometric reconfiguration through ligament bending and rotation, such as the re-entrant and star-shaped lattices, exhibit considerably higher strain amplification than architectures whose deformation is dominated by localized rotational or stretching mechanisms. Among the four auxetic architectures investigated, the star-shaped lattice consistently achieved the highest SAF, whereas the arrowheaded lattice exhibited the lowest. These findings highlight the critical role of lattice topology and deformation mechanism in governing strain amplification and provide valuable guidance for the design and selection of auxetic metamaterials for strain-amplifying applications.

To provide a broader comparison of the four auxetic architectures, Figs. 11 and 12 present Ashby-style performance maps relating the strain amplification factor (SAF) to relative density and effective Poisson's ratio, respectively. The coloured regions are schematic performance envelopes hypothesized from the finite element simulation results to illustrate the approximate design space occupied by each lattice architecture rather than representing precise performance boundaries. Together, the maps demonstrate that each auxetic topology occupies a distinct region of the performance space, reflecting the different deformation mechanisms governing its mechanical response.

Fig. 11 shows that the re-entrant and star-shaped lattices consistently occupy the high strain amplification region while maintaining relatively low relative densities, demonstrating their ability to efficiently concentrate deformation without substantially increasing structural mass. In contrast, the chiral and arrowheaded lattices remain confined to considerably lower strain amplification values despite exhibiting comparable relative densities, confirming that the observed differences in SAF are governed primarily by lattice topology and deformation mechanism rather than relative density alone.

Fig. 12 further illustrates the relationship between strain amplification and effective Poisson's ratio while simultaneously incorporating effective stiffness through the marker size. The arrowheaded lattice exhibits the most negative effective Poisson's ratio together with the largest markers, indicating the highest stiffness, but consistently occupies the low-SAF region. Conversely, the re-entrant and star-shaped lattices combine substantially higher strain amplification with comparatively less negative Poisson's ratios and lower stiffness, highlighting the inherent trade-off between deformation concentration and structural rigidity. The chiral lattice occupies an intermediate region of the performance space, providing moderate strain amplification, auxetic behaviour, and comparatively low stiffness. Unlike the bending-dominated deformation of the re-entrant and star-shaped lattices, the chiral architecture deforms primarily through rotation of circular nodes connected by compliant ligaments, producing a more distributed deformation field. Although this mechanism results in lower strain amplification, it generates smoother stress distributions that may be advantageous for applications involving repeated or cyclic loading.

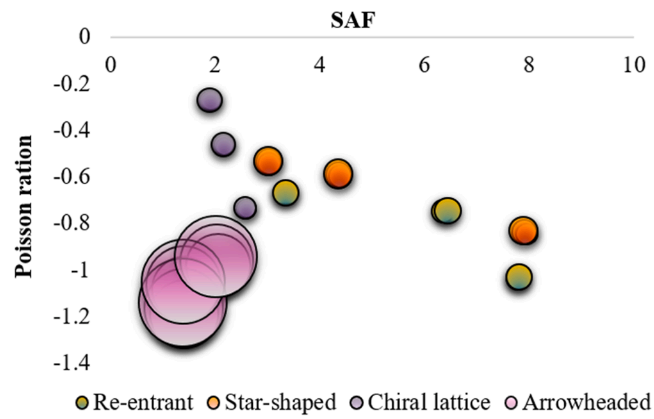


**Fig. 12.** Ashby-style performance map of SAF versus effective Poisson's ratio for the investigated auxetic lattice architectures. Bubble size represents effective stiffness, while the coloured regions indicate conceptual performance envelopes derived from the finite element simulation results.

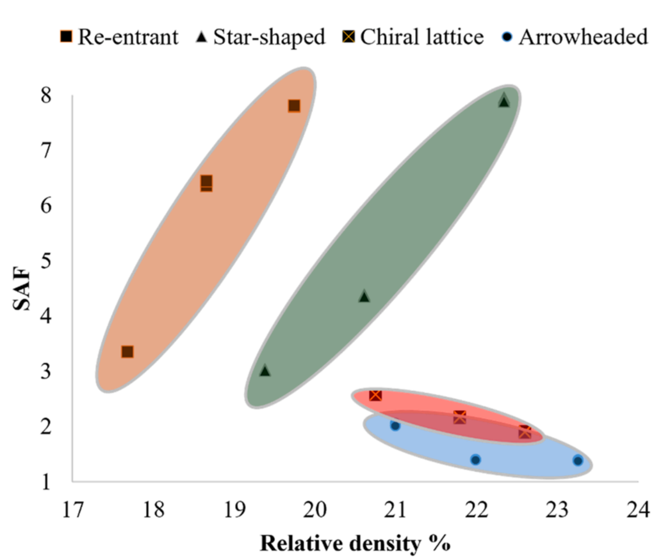


**Fig. 11.** Ashby-style performance map showing the relationship between SAF and relative density for the investigated auxetic lattice architectures.

Collectively, the two performance maps (Figs. 11 and 12) illustrate the expanded design space enabled by mechanical metamaterials, where geometric architecture can be tailored to achieve different combinations of strain amplification, auxeticity, stiffness, and lightweighting that are unattainable in conventional materials. Rather than identifying a universally superior lattice topology, the maps demonstrate that each architecture occupies a distinct region of the design space defined by its characteristic deformation mechanism. Consequently, architecture selection should be guided by the primary functional requirements of the intended application. The re-entrant and star-shaped lattices are particularly attractive for sensing, mechanochromic devices, and energy harvesting, where maximizing local strain is desirable, whereas the arrowheaded lattice is better suited to structural applications requiring high stiffness and pronounced auxetic behaviour. The chiral lattice provides an intermediate compromise between these competing characteristics, making it a promising candidate for adaptive structures and components subjected to repeated or cyclic deformation.

## 4. Future research

Although this study establishes a consistent comparative framework for evaluating representative auxetic lattice architectures, several opportunities remain for future research. First, experimental validation using additively manufactured specimens is required to verify the predicted strain amplification, effective Poisson's ratio, stiffness, and stress distributions under realistic loading conditions. Full-field measurement techniques, such as digital image correlation, would enable direct quantification of the localized deformation fields and provide further validation of the finite element predictions. The present study focused on quasi-static monotonic loading. Future investigations should therefore examine the fatigue behaviour, cyclic durability, and failure mechanisms of strain-amplifying auxetic lattices, particularly for sensing, wearable, and structural health monitoring applications where repeated loading is expected. Since high strain amplification is inherently associated with localized deformation and stress concentrations, understanding the trade-off between strain amplification, structural integrity, and long-term durability will be essential for practical implementation.

Another promising direction is the integration of strain-amplifying auxetic lattices with functional materials, including piezoresistive, piezoelectric, triboelectric, fibre-optic, and mechanochromic systems. The large, localized strains generated through geometric amplification have the potential to enhance sensing sensitivity, signal generation, and energy conversion efficiency without modifying the constituent material.

Finally, the comparative framework and Ashby-style performance maps developed in this study provide a foundation for the systematic design and optimization of auxetic metamaterials. Future work may extend the proposed methodology to 3D lattice architectures, topology-optimized and hierarchical metamaterials, and multi-material additive manufacturing. Incorporating manufacturing-induced imperfections, material anisotropy, process-dependent geometric deviations, and multi-objective optimization would further improve the predictive capability of the framework and support the development of application-specific auxetic metamaterials with tailored combinations of strain amplification, stiffness, auxeticity, and lightweighting.

## 5. Conclusions

This study presented a systematic finite element comparison of four representative auxetic lattice architectures (re-entrant, star-shaped, arrowheaded, and chiral) using a unified modelling framework based on a validated hyperelastic PBAT material model. By maintaining identical material properties, geometric scaling, boundary conditions, loading conditions, and performance evaluation metrics, the proposed framework enabled direct comparison of the intrinsic mechanical behaviour of the different lattice topologies.

The results demonstrate that lattice topology is the dominant factor governing the mechanical response of auxetic metamaterials, producing nearly a six-fold variation in strain amplification across the investigated architectures and geometric configurations. The re-entrant and star-shaped lattices consistently achieved the highest strain amplification, making them attractive for applications requiring enhanced localized deformation, such as sensing, mechanochromic devices, and energy harvesting. In contrast, the arrowheaded lattice exhibited the highest effective stiffness together with the most negative effective Poisson's ratio, but the lowest strain amplification, highlighting the trade-off between structural rigidity and deformation amplification. The chiral lattice provided an intermediate balance of strain amplification and auxetic behaviour through its rotation-dominated deformation mechanism, while also exhibiting smoother stress distributions that may be advantageous under repeated or cyclic loading.

The parametric investigation further demonstrated that the influence of geometric parameters is strongly architecture dependent. Cell angle significantly affected the mechanical response, with strain amplification varying by up to approximately 60% within individual architectures, whereas changes in out-of-plane thickness primarily increased structural stiffness with only a minor influence on strain amplification. These findings demonstrate that geometric tuning can effectively tailor mechanical performance while preserving the underlying deformation mechanisms of each lattice topology.

Finally, the proposed comparative framework and the resulting Ashby-style performance maps provide a practical multi-objective design methodology for evaluating auxetic metamaterials based on strain amplification, auxeticity, stiffness, relative density, and stress distribution simultaneously. Rather than identifying a universally optimal architecture, this study demonstrates that each lattice topology occupies a distinct region of the mechanical design space, enabling application-specific selection according to the required balance between deformation amplification, structural performance, and material efficiency. These findings provide quantitative design guidance for the development of next-generation auxetic metamaterials for sensing, adaptive structures, energy harvesting, and other multifunctional engineering applications.


## Funding

This research received partial funding from Ajman University (grant agreement 2025-IRG-CEIT-13) and the NWO (Dutch Research Council, Vidi TTW, File number 21226). The data essential for supporting the conclusions are presented within the paper.


## CRediT authorship contribution statement

**Sakineh Fotouhi:** Writing – review & editing, Writing – original draft, Supervision, Methodology, Investigation, Formal analysis, Conceptualization. **Fahad Mohammed:** Writing – original draft, Validation, Methodology, Investigation, Conceptualization. **Fadi Jaber:** Writing – review & editing, Writing – original draft, Methodology, Investigation, Funding acquisition, Conceptualization. **Mohammad Fotouhi:** Writing – review & editing, Writing – original draft, Supervision, Methodology, Funding acquisition, Conceptualization.

## Declaration of competing interest

The authors declare that they have no known competing financial interests or personal relationships that could have appeared to influence the work reported in this paper.


## Acknowledgments

Not applicable.


## Data availability

Data will be made available on request.

## References


[1] K. Bertoldi, V. Vitelli, J. Christensen, M. Van Hecke, Flexible mechanical metamaterials, Nat. Rev. Mater. 2 (11) (2017) 1–11.

[2] J.B. Berger, H.N. Wadley, R.M. McMeeking, Mechanical metamaterials at the theoretical limit of isotropic elastic stiffness, Nature 543 (7646) (2017) 533–537.

[3] X. Zheng, H. Lee, T.H. Weisgraber, M. Shusteff, J. DeOtte, E.B. Duoss, J.D. Kuntz, M.M. Biener, Q. Ge, J.A. Jackson, S.O. Kucheyev, N.X. Fang, C.M. Spadaccini, Ultralight, ultrastiff mechanical metamaterials, Science 344 (6190) (2014) 1373–1377.

[4] C. Coulais, E. Teomy, K. de Reus, Y. Shokef, M. van Hecke, Combinatorial design of textured mechanical metamaterials, Nature 535 (7613) (2016) 529–532.

[5] R. Craster, S. Guenneau, M. Kadic, M. Wegener, Mech. Metamater. Rep. Prog. Phys. 86 (9) (2023).

[6] R. Lakes, Foam structures with a negative Poisson's ratio, Science 235 (1987) 1038–1040.

[7] M. Periyasamy, N. Srinivasan, A review on auxetic structures: applications, properties, classifications, finite element analysis, manufacturing methods, and selective laser melting process parameters, Results. Eng. 28 (2025) 107660.

[8] K. Evans, M. Nkansah, I. Hutchinson, et al., Molecular network design, Nature 353 (1991) 124.

[9] H.M. Kolken, A.A. Zadpoor, Auxetic mechanical metamaterials, RSC. Adv. 7 (9) (2017) 5111–5129.

[10] Y. Zhang, W.Z. Jiang, W. Jiang, X.Y. Zhang, J. Dong, Y.M. Xie, K.E. Evans, X. Ren, Recent advances of auxetic metamaterials in smart materials and structural systems, Adv. Funct. Mater. 35 (2025) 2421746.

[11] P.U. Kelkar, H.S. Kim, K.H. Cho, J.Y. Kwak, C.Y. Kang, H.C. Song, Cellular auxetic structures for mechanical metamaterials: a review, Sensors 20 (11) (2020) 3132.

[12] D.B. Ercument, Y.H. Elmoghazy, Z. Al Mahmoud, B. Safaei, S. Sahmani, J. Petrů, Mechanical behaviour and energy absorption performance of modified anti-tri chiral novel auxetic structures through experimental and numerical analysis subjected to surrogate metamodeling, Results. Eng. 29 (2026) 108967.

[13] A. Alderson, K.L. Alderson, Auxetic materials. Proceedings of the Institution of Mechanical Engineers, part G, J. Aerosp. Eng. 221 (4) (2007) 565–575.

[14] X. Ren, R. Das, P. Tran, T.D. Ngo, Y.M. Xie, Auxetic metamaterials and structures: a review, Smart. Mater. Struct. 27 (2) (2018) 023001.

[15] M. Sengul, H.A. Tasdemir, A. Tamer, 2025. Real-world applications of auxetic structures in engineering: a review, Structures 80 (2025) 109673.
[16] N. Kim, S. Park, M.C. Kim, Y.W. Choi, Auxetic crack-based wearable strain sensor designed for sustainable conformal contact, Sens. Actuat. A 387 (2025) 116429.
[17] X. Liu, W. Wang, X. Wang, Y. Zhou, L. Li, L. Xing, W. Zhang, O. Yue, Efficient triboelectric nanogenerators with on-demand auxetic structure achieving deformation matching in wearable devices, Nano. Energy 135 (2025) 110648.
[18] D. Jiang, H. Thissen, T.C. Hughes, K. Yang, R. Wilson, A.B. Murphy, V. Nguyen, Advances in additive manufacturing of auxetic structures for biomedical applications, Mater. Today. Commun. 40 (2024) 110045.
[19] H.Y. Lee, M. Gu, J. Hwang, H. Hwang, Y.S. Kim, S.Y. Lee, S.H. Kim, Auxetic photonic patterns with ultrasensitive mechanochromism, Adv. Sci. 11 (2024) 2304022.
[20] C. Tang, Fundamental aspects of stretchable mechanochromic materials: fabrication and characterization, Materials 17 (2024) 3980.
[21] R. Lin, D. Kou, L. Gao, S. Li, Z. Gao, X. Li, W. Ma, S. Zhang, Biomimetic photonic elastomer exhibiting stress/moisture reconfigurable wrinkle-lattice for reversible deformation information storage, ACS. Nano 18 (20) (2024) 13346–13360.
[22] J.H. Shin, H.J. Yang, J.Y. Park, S.H. Han, D. Kim, S. Nam, S.S. Choi, Optimized and uniform strain control in intrinsic stretchable mechanochromic materials with color- and polarization-separating encryption using kirigami cuts and rigid strain-stoppers, Adv. Funct. Mater. 35 (2025) 2570138.
[23] J. Li, Y. Ma, Z. Zhao, Z. Zheng, J. Gao, J. Hao, J. Yang, B. Zhang, J. Hu, Bioinspired integrated auxetic conductive elastomer composite with high stretchability and robust interface, Small 21 (2025) 2504272.
[24] M. Gulzari, S. Sornsomrit, M.A. Akbar, S. Rudykh, Influence of geometric design on mechanical performance of auxetic metastructure, Adv. Eng. Mater. 28 (2026) e70954.
[25] W. Wang, X. Wang, L. Li, et al., Bioinspired auxetic metastructures enable biomechanically adaptive, machine learning-enhanced self-powered sensing with ultrahigh efficiency, Nano-Micro. Lett. 18 (2026) 286.
[26] R. Zhao, Y. He, Y. He, Z. Li, M. Chen, N. Zhou, G. Tao, C. Hou, Dual-mode fiber strain sensor based on mechanochromic photonic crystal and transparent conductive elastomer for human motion detection, ACS. Appl. Mater. Interfac. 15 (12) (2023) 16063–16071.
[27] Mohammed F, Akbar J, Soe S, Atkinson G, Fotouhi S Fear-inspired strain amplification layers for composite structures. In: Proceedings of the 22nd European Conference on Composite Materials (ECCM22). Oslo, Norway; 2026.
[28] V. Siniauskaya, H. Wang, Y. Liu, Y. Chen, M. Zhuravkov, Y. Lyu, A review on the auxetic mechanical metamaterials and their applications in the field of applied engineering, Front. Mater. 11 (2024) 1453905.
[29] Y. Schneider, V. Guski, S. Schmauder, J. Kadkhodapour, J. Hufert, A. Grebhardt, C. Bonten, Deformation behavior investigation of auxetic structure made of poly (butylene adipate-co-terephthalate) biopolymers using finite element method, Polymers 15 (7) (2023) 1792.
[30] M.H. Fu, O.T. Xu, L.L. Hu, T.X. Yu, Nonlinear shear modulus of re-entrant hexagonal honeycombs under large deformation, Int. J. Solids. Struct. 80 (2016) 284–296.
[31] H. Wan, H. Ohtaki, S. Kotosaka, G. Hu, A study of negative Poisson's ratios in auxetic honeycombs based on a large deflection model, Eur. J. Mech. Solids 23 (1) (2004) 95–106.
[32] K.E. Evans, Auxetic polymers: a new range of materials, Endeavour 15 (4) (1991) 170–174.
[33] J. Zhang, G. Lu, Energy absorption of re-entrant honeycombs in tension and compression, Eng. Struct. 288 (2023) 116237.
[34] F. Mustahsan, S.Z. Khan, A.A. Zaidi, Y.H. Alahmadi, E.R. Mahmoud, H. Almohamadi, Re-entrant honeycomb auxetic structure with enhanced directional properties, Materials 15 (22) (2022) 8022.
[35] Y. Chen, X.N. Liu, G.K. Hu, Q.P. Sun, Q.S. Zheng, Micropolar continuum modelling of bi-dimensional tetrachiral lattices, Proc. Math. Phys. Eng. Sci. 470 (2165) (2014) 20130734.
[36] A. Spadoni, M. Ruzzene, Elasto-static micropolar behavior of a chiral auxetic lattice, J. Mech. Phys. Solids. 60 (1) (2012) 156–171.
[37] I. Ali, Y.J. Jun, Mathematical models for in-plane moduli of honeycomb structures: a review, Res. J. Appl. Sci. Eng. Technol. 7 (3) (2014) 581–592.